



# Real-time microrobot posture recognition via biplane X-ray imaging system for external electromagnetic actuation

Phu Bao Nguyen<sup>1</sup> · Byungjeon Kang<sup>2</sup> · D. M. Bappy<sup>2</sup> · Eunpyo Choi<sup>1</sup> · Sukho Park<sup>3</sup> · Seong Young Ko<sup>1</sup> · Jong-Oh Park<sup>1</sup> · Chang-Sei Kim<sup>1</sup> 

Received: 24 April 2018 / Accepted: 3 August 2018  
© CARS 2018

## Abstract

**Purpose** As a promising intravascular therapeutic approach for autonomous catheterization, especially for thrombosis treatment, a microrobot or robotic catheter driven by an external electromagnetic actuation system has been recently investigated. However, the three-dimensional (3D) real-time position and orientation tracking of the microrobot remains a challenge for precise feedback control in clinical applications owing to the micro-size of the microrobot geometry in vessels, along with bifurcation and vulnerability. Therefore, in this paper, we propose a 3D posture recognition method for the unmanned microrobotic surgery driven by an external electromagnetic actuator system.

**Methods** We propose a real-time position and spatial orientation tracking method for a millimeter-sized intravascular object or microrobot using a principal component analysis algorithm and an X-ray reconstruction. The suggested algorithm was implemented to an actual controllable wireless microrobot system composed of a bullet-shaped object, a biplane X-ray imaging device, and an electromagnetic actuation system. Numerical computations and experiments were conducted for the performance verification.

**Results** The experimental results showed a good performance of the implemented system with tracking errors less than 0.4 mm in position and 2° in orientation. The proposed tracking technique accomplished a fast processing time, ~0.125 ms/frame, and high-precision recognition of the micro-sized object.

**Conclusions** Since the suggested method does not require pre-information of the object geometry in the human body for its 3D shape and position recognition, it could be applied to various elliptical shapes of the microrobot system with computation time efficacy and recognition accuracy. Hence, the method can be used for therapeutic millimeter- or micron-sized manipulator recognition in vascular, as well as implanted objects in the human body.

**Keywords** Real-time 3D posture recognition · Intravascular microrobot · Electromagnetic actuation system · Principal component analysis · X-ray reconstruction

## Introduction

Over the past decade, cardiovascular diseases have increased significantly and have become the major contributors to morbidity and mortality [1]. In particular, occlusive thrombus in the arteries or veins of a blood clot causes partial or complete blockages of circulation in the patient's body, leading to pain or possibly death; thus, treatments such as anticoagulant drugs and angioplasty are critical for survival. Among them, catheterization is widely used along with anticoagulant drugs to remove or dissolve the clot [2]. However, in a review by Bashir et al., catheter-directed thrombolysis (CDT) was reported to frequently cause thrombolytic bleeding at the surgical position during operation, especially when used in

---

✉ Jong-Oh Park  
jop@jnu.ac.kr

✉ Chang-Sei Kim  
ckim@jnu.ac.kr

<sup>1</sup> School of Mechanical Engineering, Chonnam National University, Gwangju 61186, South Korea

<sup>2</sup> Medical Microrobot Center, Robot Research Initiative, Chonnam National University, Gwangju 61186, South Korea

<sup>3</sup> Department of Robotics Engineering, Daegu Gyeongbuk Institute of Science and Technology, Daegu 42988, South Korea

combination with anticoagulant drugs. Therefore, CDT is recommended only to patients with low bleeding risks [3]. Furthermore, Bowdle [4] reported that a guide wire catheter may occasionally cause internal venous injury or the guide wire may become trapped against the wall of the blood vessel during insertion through the internal jugular vein. The limitations of the guide wire catheter technique, therefore, necessitate the development of a new method for thrombosis surgery.

As a promising method for robotic catheter therapeutics, a controllable wireless microrobot (CWM) system with a less invasive intra-operative procedure has been proposed for thrombus treatment [5]. The CWM utilizes an electromagnetic actuator (EMA) system for microrobot actuation and a biplane X-ray system for microrobot imaging. However, due to an insufficient X-ray imaging processing algorithm of extracting spatial position and orientation information from the microrobot image in the vascular, the microrobot could not be precisely controlled and may cause damage, and ultimately advanced autonomous control methods have not yet been realized.

Recently, several researchers have conquered the challenges of microrobot tracking [2, 5–8]. Various types of imaging techniques for estimating thrombus age were analyzed in [2], in which the goal was to gather and evaluate clinical data relating to imaging modalities. In [5], different types of localization methods were discussed for a microrobot, such as computed tomography (CT), positron emission tomography (PET), and ultrasound. A ferromagnetic microcapsule steering and navigation using MRI was presented in [6] using Frangi vesselness filtering from MRI images, before guiding the microrobot from the injection point to the tumor with the fast marching method (FMM). Finally, depending on the predefined path, navigation was performed along a 3D path via a model predictive controller (MPC). According to [7], a combination of condensation tracking and the Hough transform allows for the efficient and accurate real-time tracking of surgical instruments. The authors of [8] proposed an extended Kalman filter (EKF) to precisely track the catheter paths.

However, previous algorithms utilizing X-ray imaging have several limitations that affect the precision of the 3D reconstruction, as well as the microrobot tracking performances caused by the image processing parametric errors from the manual measurements of the system configuration parameters, 3D reconstruction processing time, system setup requirement of the X-ray tube, and detector alignment.

In this paper, we propose a technique that enables the precise tracking of the position and orientation of the microrobot in real time. The developed algorithm based on principal component analysis (PCA) is applied to a CWM system consisting of a bullet-shaped microrobot, a biplane X-ray imaging device, and an EMA system. In addition, we applied

the proposed algorithm to seven different shapes of microrobots, previously researched as cardiovascular intervention candidates, to show the practical applicability to different geometries of millimeter- and micrometer-sized elliptical objects. The proposed technique showed superior accuracy and a faster processing time compared to the other relevant methodologies described in [9–14]. Our proposed method uses features extracted by the PCA algorithm from X-ray images to track the microrobot in real time. In comparison, [9] introduced a centerline method using CT images for navigating the intravascular microrobot, whereas in [10] the authors reconstructed a 3D volume using ultrasound images and attached a sensor together with the catheter tip for tracking. Learning-based 3D orientation of an object from a single image, and the application to a robotic arm for grasping, were discussed in [11]. According to [12], a 3D tracking system was developed using two high-speed vision systems where the object position and orientation were reconstructed by applying epipolar geometry. An ultrasound image-based system was used for real-time tracking of the endovascular device in [13], where a control algorithm processes the ultrasound images in real time and detects the device for position control. Finally, the authors in [14] presented a semiautomatic model-based tracking to track foot bones, which show the better accuracy with the expense of high computation time.

The primary contributions in this study are that the computer-recognizable image processing method derived from the PCA algorithm and biplane X-ray image was realized for an actual system for further medical millimeter- or micro-sized robot applications, especially in cardiovascular intervention. The image processing time was significantly reduced, enabling the fast tracking of the microrobot in real time for a precise intra-operative control; an improvement in the posture tracking accuracy for the micro-sized object; and a small resultant geometric error regardless of the external device setup, such as the distance from the X-ray tube to an object and the microrobot shape. These are essential technical advances for the autonomous microrobotic surgery and remotely controlled medical robotic system.

## Methods

First, we capture the stereo images of the microrobot using biplane X-ray. Next, a segmentation algorithm is applied to the microrobot area in two-dimensional (2D) images to parse the image into point clouds in the 2D plane for each stereo image. Subsequently, the point clouds are processed using the PCA algorithm to extract the feature points consisting of the center and tips of the microrobot. To match the correct correspondence of each point set of each plane image, an epipolar geometry and a root-mean-square deviation (RMSD)-based

technique are used. Finally, the set of corresponding points are reconstructed so that the computer can determine and recognize the position and orientation of the microrobot in 3D space.

### PCA algorithm to extract the tip and center points from 2D images

Figure 1a depicts the coordinate system of the target system. Through two perpendicular X-ray devices, we can obtain two 2D plane images simultaneously. Since the microrobot has two endpoints, the object shape is projected onto two 2D planes consistent with the robot’s direction in 3D space. Figure 1b shows an example of the captured image by the biplane X-ray imaging device and a real photograph of the microrobot. Its shape is considered as an ellipse, and the geometry can be characterized in terms of two principal components: major and minor axes, as illustrated in Fig. 1c. For this shape recognition, several methods can be used to extract the geometric parameters from an ellipse-like object, such as ellipse fitting, least square fitting, and PCA with wavelet transform or clustering fitting [15, 16]. However, owing to the slow computation time and large computational burden, those methods are not appropriate for tracking microrobots in real time [17]. To overcome those problems, the PCA algorithm is used in this study to extract the center and endpoints of the microrobot from 2D images [18]. The center and endpoints are the base shape information for the latter image processing.

For the extraction of both endpoints, the PCA algorithm is applied to the 2D segmented image of the microrobot, as shown in Fig. 1b. The point cloud is denoted by  $\chi$ , which consists of  $n$  data points in terms of the  $x$ - and  $y$ -components as follows:

$$\chi = \begin{bmatrix} x(1) & y(1) \\ \vdots & \vdots \\ x(n) & y(n) \end{bmatrix} \tag{1}$$

where  $\chi(k) = [x(k) \ y(k)]$  represents the  $k$ th point in the point cloud. Subsequently, the center of this point cloud  $C(\bar{x}, \bar{y})$ , which is considered as the centroid of the microrobot projected onto the X-ray image, is determined by the mean of all these points in both the  $x$ - and  $y$ -direction in the following equation:

$$C(\bar{x}, \bar{y}) = [\bar{x}, \bar{y}] = \left[ \frac{\sum_{k=1}^n x(k)}{n}, \frac{\sum_{k=1}^n y(k)}{n} \right]. \tag{2}$$

Further, both the endpoints of the microrobot image,  $m_1$  and  $m_2$ , can be determined by

$$\begin{cases} m_1 = (2v_1\sqrt{\lambda_1} + \bar{x}, 2v_2\sqrt{\lambda_1} + \bar{y}) \\ m_2 = (-2v_1\sqrt{\lambda_1} + \bar{x}, -2v_2\sqrt{\lambda_1} + \bar{y}) \end{cases} \tag{3}$$

where  $\lambda_{1,2} = \frac{1}{2} \left( \sigma_{11} + \sigma_{22} \pm \sqrt{(\sigma_{11} - \sigma_{22})^2 + 4\sigma_{12}^2} \right)$  are the eigenvalues of the point cloud matrix  $\chi$ ,  $v_1 = \frac{\sigma_{12}}{\sqrt{(\lambda_1 - \sigma_{11})^2 + \sigma_{12}^2}}$  and  $v_2 = \frac{\lambda_1 - \sigma_{11}}{\sqrt{(\lambda_1 - \sigma_{11})^2 + \sigma_{12}^2}}$  are the respective eigenvectors determined relative to their covariances  $\sigma_{11} = \frac{1}{n-1} \sum_{k=1}^n [x(k)]^2$ ,  $\sigma_{22} = \frac{1}{n-1} \sum_{k=1}^n [y(k)]^2$ , and  $\sigma_{12} = \sigma_{21} = \frac{1}{n-1} \sum_{k=1}^n x(k) \cdot y(k)$ .

Figure 1c shows the center and tip points of the microrobot extracted by the PCA algorithm. Using the PCA algorithm, two sets of 2D plane points are obtained from a pair of the corresponding X-ray images. Each set contains three points as two endpoints ( $m_1, m_2$ ) and a center point,  $C(\bar{x}, \bar{y})$ , of the microrobot. These points are utilized to reconstruct the geometric shape of the object.

### Position reconstruction

An X-ray reconstruction technique is applied to reconstruct the microrobot position in the 3D space from the two sets of point data gathered by the PCA algorithm. As proposed in our previous work [19], it is assumed that two points  $m_p = [u_p \ v_p]^T$  and  $m_q = [u_q \ v_q]^T$  are 2D points, in which a 3D point  $M = [X \ Y \ Z \ 1]^T$  in the world coordinate system is projected onto two X-ray images, named  $p$ - and  $q$ -image, respectively. Throughout the present work, the notations  $p$  and  $q$  are used to describe two corresponding X-ray images.

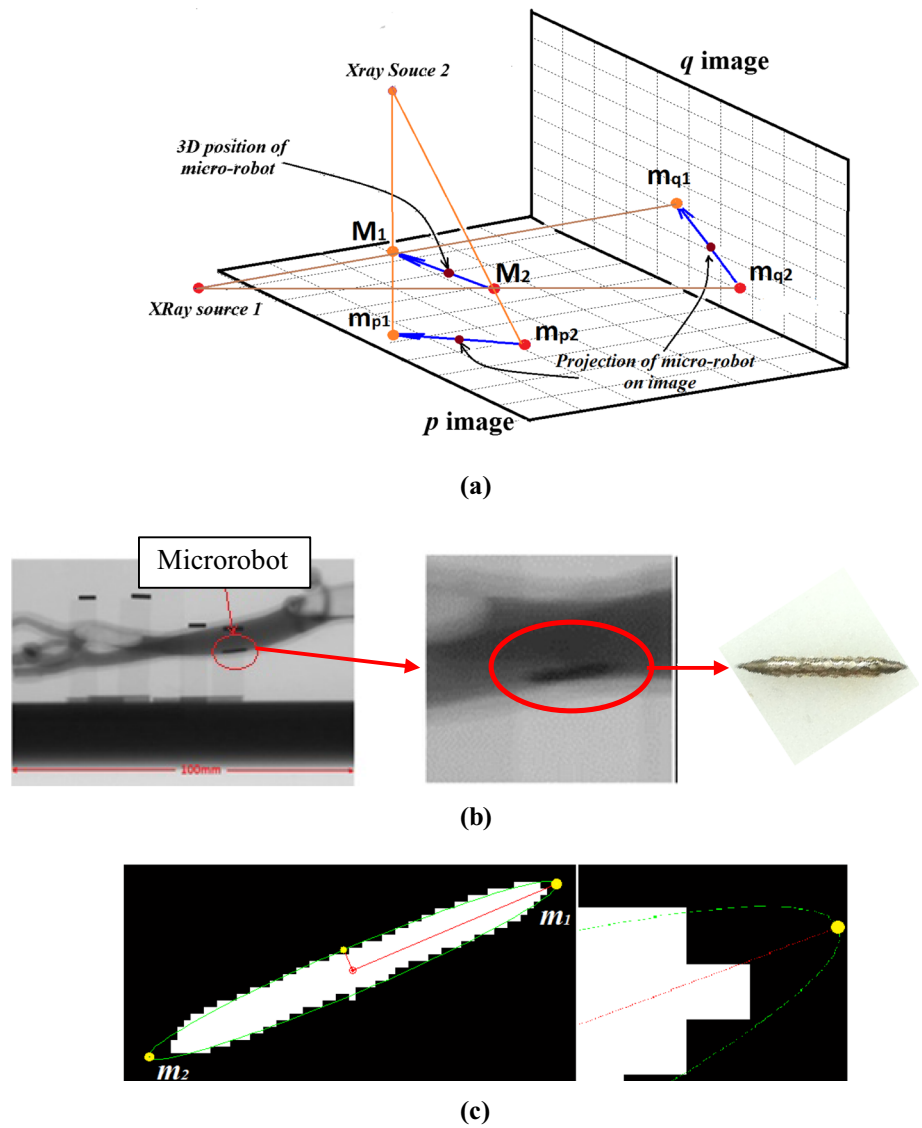
The projection from a 3D point,  $M(X, Y, Z)$ , to a 2D point,  $m(u, v)$ , is described by the projection equation as follows:

$$\lambda_p \begin{bmatrix} u \\ v \\ 1 \end{bmatrix} = \begin{bmatrix} f_1 & s & c1 & 0 \\ 0 & f_2 & c2 & 0 \\ 0 & 0 & 1 & 0 \end{bmatrix} \begin{bmatrix} R^{3 \times 3} & t^{3 \times 1} \\ 0 & 0 & 0 & 1 \end{bmatrix} \begin{bmatrix} X \\ Y \\ Z \\ 1 \end{bmatrix} \tag{4}$$

where  $f_1$  and  $f_2$  are the focal lengths of the camera with the camera center ( $c1, c2$ ), and  $s$  is a skew factor obtained from camera calibration. By calibration and solving Eq. (4) with the triangulation relation, the position of  $M$  in the global coordinate system is obtained by solving the following equation:

$$\begin{aligned} M_{\text{homo}} &= H^{-1} \cdot M' \\ M &= M_{\text{homo}} / M_{\text{homo}_{41}} \end{aligned} \tag{5}$$

**Fig. 1** **a** Coordinate system for the microrobot image recognition, **b** X-ray images of the intravascular microrobot, and **c** major and minor axes of the microrobot image



where  $H$  is a  $4 \times 4$  infinity homography matrix [20],  $M_{\text{homo}(4 \times 1)}$  is a reconstructed 3D point in the homogeneous coordinate system, and  $M'$  is reconstructed 3D points in the first X-ray coordinate system. By dividing  $M_{\text{homo}}$  by its fourth component ( $M_{\text{homo}_41}$ ), we can obtain point  $M$  in the global coordinate system. Let  $K_q$  be the X-ray intrinsic matrix of the  $q$ -plane obtained from the X-ray calibration and  $B_{3 \times 4} = P_q \cdot H^{-1}$ ; then, we obtain the following transformed matrix:

$$M' = \lambda_p \cdot [m_p^T \quad 1/\lambda_p]^T \quad \text{and} \quad \lambda_p = \frac{u_q \cdot B_{2,4} - v_q \cdot B_{1,4}}{(B_{1,1} \cdot u_p + B_{1,2} \cdot v_p + B_{1,3}) \cdot v_q - u_q \cdot (B_{2,1} \cdot u_p + B_{2,2} \cdot v_p + B_{2,3})} \quad (6)$$

where  $\lambda_p$  is the projection scale factor of the  $p$ -view that is computed by incorporating the  $q$ -plane images. By substituting these parameters into Eq. (5), the 3D position of point  $M$

is reconstructed from the corresponding X-ray images from the  $p$ - and  $q$ -planes.

Using two corresponding center points from two images,  $C_p(\bar{x}_p, \bar{y}_p)$  and  $C_q(\bar{x}_q, \bar{y}_q)$ , obtained from the PCA algorithm explained in “PCA algorithm to extract the tip and center points from 2D images” section as well as Eqs. (5) and (6), the centroid of the microrobot is reconstructed in 3D

space. In this computation, the position of the microrobot is determined with respect to the world coordinate system in 3D space.

### Orientation reconstruction

To reconstruct the orientation of the microrobot, two pairs of tip points are extracted from two images using the PCA algorithm. These four points are denoted as  $m_{p1}$  and  $m_{p2}$  from the  $p$ -image, and  $m_{q1}$  and  $m_{q2}$  from the  $q$ -image. Using these four points, we identify the correct corresponding point pair and their constraints among the four points with respect to the real posture reconstruct of the tip points. Two combination cases are possible:

- Case A  $m_{p1}$  is the correspondence of  $m_{q1}$ , and  $m_{p2}$  is the correspondence of  $m_{q2}$
- Case B  $m_{p1}$  is the correspondence of  $m_{q2}$ , and  $m_{p2}$  is the correspondence of  $m_{q1}$

Here, the epipolar geometry along with the fundamental matrix is used to determine the direction and to check the correct corresponding point pair.

### Epipolar geometry and fundamental matrix

Figure 2 describes the epipolar geometry between two corresponding images  $p$  and  $q$ , relative to the epipolar plane and epipolar line. The epipolar constraint is used to determine whether a point  $m_p$  in image  $p$  is the correspondence of  $m_q$  in image  $q$ . An epipolar constraint between two corresponding points  $m_p$  and  $m_q$  projected from one 3D point  $M$  is described by a fundamental matrix. All pairs of corresponding points should meet the following constraint:

$$m_p^T \mathcal{F} m_q = 0 \tag{7}$$

where  $\mathcal{F}$  is the fundamental matrix and  $\mathcal{F} m_q$  describes the epipolar line on which the corresponding point  $m_p$  must lie.

The fundamental matrix is obtained via the Hartley and Zisserman approaches in [20]. First, suppose that the intrinsic and extrinsic parameters of the biplane X-ray imaging device are properly obtained from the calibration process with a checkerboard [19] and that they are denoted as  $K_p$  and  $[R_p|t_p]$  for image  $p$  and  $K_q$  and  $[R_q|t_q]$  for image  $q$ . Furthermore,  $P_p$  and  $P_q$  are the  $3 \times 4$  projection matrices of two views of  $p$  and  $q$ , respectively, that are obtained from the following equation:

$$\begin{cases} P_p = K_p [R_p | t_p] \\ P_q = K_q [R_q | t_q] \end{cases} \tag{8}$$

where  $K_i$  is a  $3 \times 3$  upper triangular matrix that describes the intrinsic parameter of the  $i$ th X-ray view, and  $[R_i|t_i]$  is a  $4 \times 3$  transformation matrix from the world coordinate system to the X-ray coordinate system in which  $i = \{p, q\}$ . Assuming

that the world coordinate system coincides with the X-ray coordinate system of the view  $p$ ,  $P_p$  and  $P_q$  become

$$\begin{cases} P_p = K_p [I | 0_{3 \times 1}] \\ P_q = K_q [R | t] \end{cases} \tag{9}$$

where  $[R|t]$  is the transformation matrix from the X-ray coordinate system of view  $p$  to that of view  $q$ . Subsequently, the fundamental matrix corresponding to two views of the biplane X-ray is computed to obtain the direction of the object in 2D from the known values of the intrinsic and extrinsic matrices.

### Direction determination

The point  $m_p$  of image  $p$  corresponds to  $m_q$  in image  $q$  if and only if the constraint  $m_p^T \mathcal{F} m_q = 0$  is valid. In theory, the corresponding point pair can be determined by checking whether the constraint is zero. However, since the error in the calibration is not the same as that in the ideal system, we proposed a root-mean-square (RMS) method to check for correct or incorrect constraints between two point pairs. This method avoids computational determination confusion and is adaptive with various cases of error in automatic processing.

For the possible combinations of the correspondence as proposed in the beginning of “Orientation reconstruction” section, we denoted these two cases of correspondence as “A” and “B,” respectively. Subsequently, by applying the constraint  $\Delta_{\alpha\beta} = m_{p\alpha}^T \mathcal{F} m_{q\beta}$  to cases A and B, where  $\alpha = \{1, 2\}$  is the index of the tip points in the 2D images, and  $\beta = \{p, q\}$  denotes the image planes, we obtain the following determinant measure:

- Case A  $\Delta_{1A} = m_{p1}^T \mathcal{F} m_{q1}$  and  $\Delta_{2A} = m_{p2}^T \mathcal{F} m_{q2}$
- Case B  $\Delta_{1B} = m_{p1}^T \mathcal{F} m_{q2}$  and  $\Delta_{2B} = m_{p2}^T \mathcal{F} m_{q1}$

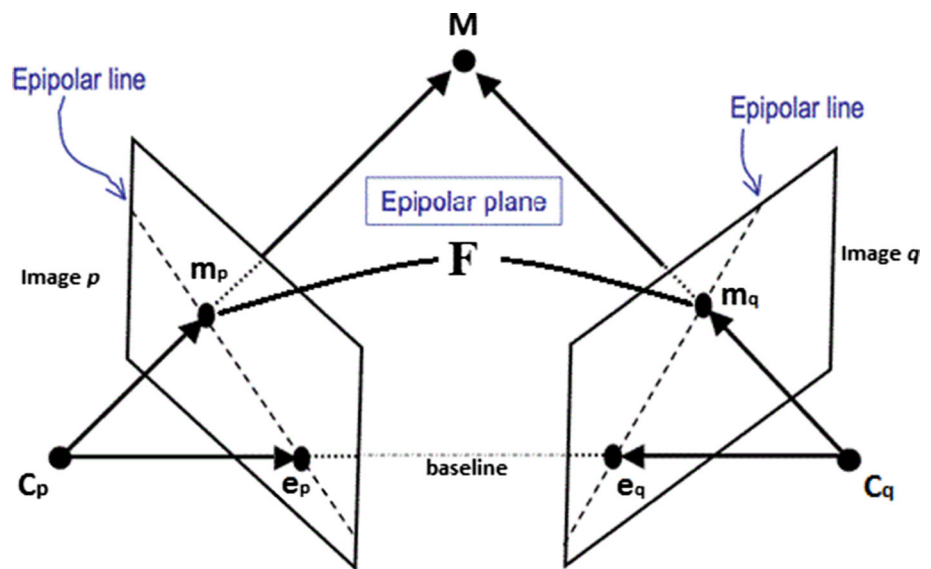
The RMS deviation (RMSD) around the expected value  $\bar{\Delta}$  with respect to the estimated parameters  $\Delta_{iA}$  and  $\Delta_{iB}$ , where  $i = \{1, 2\}$  for both cases A and B are:

$$RMSD_{A,B} = \sqrt{\frac{(\bar{\Delta} - \Delta_{1A,B})^2 + (\bar{\Delta} - \Delta_{2A,B})^2}{2}}. \tag{10}$$

The expected value  $\bar{\Delta}$  could be set equal to zero, but for the practical implementation, we set  $\bar{\Delta}$  less than  $10^{-4}$  to maintain proper precision of the results. As the natural properties of the epipolar geometry and fundamental matrix [20], if case A is the correct correspondence, then  $RMSD_B \gg RMSD_A \approx 0$  is valid, and if case B is the correct direction, then  $RMSD_A \gg RMSD_B \approx 0$  is valid.

By applying the RMSD-based checking technique to cases A and B, the correct constraint between two point pairs

**Fig. 2** Epipolar geometry between two corresponding pairs of X-ray images



$(m_{p1}, m_{q1})$  and  $(m_{p2}, m_{q2})$  can be properly determined. Furthermore, three points are lying on the major axis of the microrobot, in which two endpoints and one center point are reconstructed with respect to the world coordinate system by applying an X-ray reconstruction from Eqs. (5) and (6) from the point pairs  $(m_{p1}, m_{q1})$ ,  $(m_{p2}, m_{q2})$ , and  $(C_1, C_2)$ . The orientation in space can be determined by the vector drawn between two endpoints of the microrobot. Finally, both the position and orientation of the microrobot in the 3D space are determined.

### Reconstruction of the microrobot posture

The posture information of the microrobot in 3D space is derived from the following equation, where  $M_1$  and  $M_2$  are the reconstructed 3D points of the microrobot tip with centroid  $C$ :

$$\begin{cases} M_1 C = M_1(x_1, y_1, z_1) - C(\bar{x}, \bar{y}, \bar{z}) \\ M_2 C = M_2(x_2, y_2, z_2) - C(\bar{x}, \bar{y}, \bar{z}) \end{cases} \quad (11)$$

Here,  $M_1 C$  and  $M_2 C$  are the vectors that indicate the posture of the microrobot in the 3D space. Because the outcome of the reconstruction is the numerical posture values of the microrobot in the vascular, advanced algorithms, such as robot motion tracking and autonomous control for the microrobot navigation system, could be accomplished.

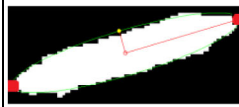
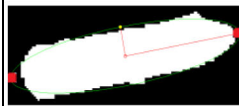
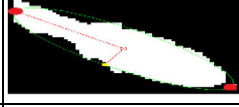
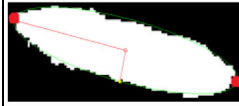
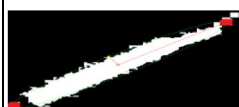
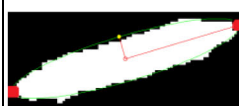
### Experimental results

To verify the accuracy and reliability of the proposed technique, we compared the reconstructed posture values from the X-ray image with reference measurements from an

optical tracking system (OTS) (Polaris Spectra, Northern Digital Inc.) of which the position measurement accuracy is 0.19 mm. We conducted experiments using seven types of microrobots with different geometric shapes listed in Table 1. The algorithm was implemented with an Intel®Core™ i7-2600 computer, CPU 2.4-GHz processor, and 8192 MB of RAM. Figure 3 shows a schematic diagram of the experimental verification of the proposed algorithm. The distance from the X-ray tube to the object was set to approximately 500 mm. Figure 3d illustrates the FOV ( $150 \text{ mm} \times 130 \text{ mm}$ ) of the biplane X-ray system together with the phantom area ( $150 \text{ mm} \times 100 \text{ mm}$ ), which ensures that the tips of the microrobot always stay inside the view [21]. First, the X-ray coordinate system was registered with the OTS coordinate system using the OTS markers attached to the X-ray tube [22–24]. A bullet-shaped microrobot was fixed inside the workspace of the biplane X-ray. The X-ray images of the microrobot were captured using an X-ray device and processed by algorithm. After the position and orientation of the microrobot were obtained, we precisely measured the tip positions (two endpoints) of the microrobot from the OTS measurements, shown in Fig. 3c. Furthermore, the position and orientation measurements were compared with the proposed technique. Each posture of the seven individual microrobots was measured at least 30 times.

The intravascular microrobot candidates and results of the suggested methodology are summarized in Table 1. Depending on the microrobot geometry and noise effect, 2–3 to 8–9 pixel differences compared to the actual size were observed. However, if we consider the actual size of the micro-object, these pixel differences could be ignored. The results show that the suggested method can successfully detect and recognize the 3D shape of the microrobot. Figure 4 shows the posture differences between the proposed technique and

**Table 1** Shape recognition results for the various shape of the microrobot including catheter tip

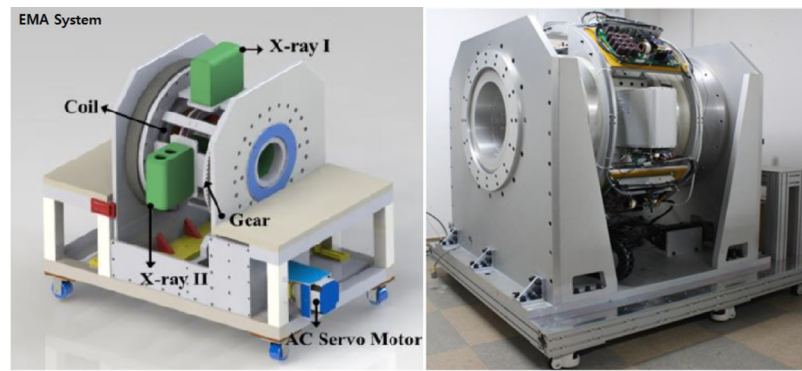
Types of microrobot		Geometric parameters ( $L, D, \alpha$ )	Reconstructed image	No. of clouding points	Errors in pixels	Processing time [ms]	
#	Real image						Material
1		NdFeB	10 mm, 2 mm, 20°		~ 500	3 ~ 4	~ 0.02
2		NdFeB	15 mm, 1.5 mm, 30°		~ 550	4 ~ 5	~ 0.02
3		NdFeB, VeroClear	19 mm, 2 mm, 15°		~ 950	8 ~ 10	~ 0.05
4		NdFeB	3 mm, 1.5 mm, 30°		~ 250	3 ~ 4	~ 0.018
5		NdFeB	15 mm, 1.5 mm, 20°		~ 550	2 ~ 3	~ 0.02
6		NdFeB, VeroWhite	30 mm, 5 mm, 15°		~ 3750	8 ~ 10	~ 0.125
7		NdFeB	8 mm, 1 mm, 20°		~ 200	2 ~ 3	~ 0.017

OTS measurements, with a position error of approximately 0.2–0.4 mm and orientation error of 1°–2° for all types of microrobots.

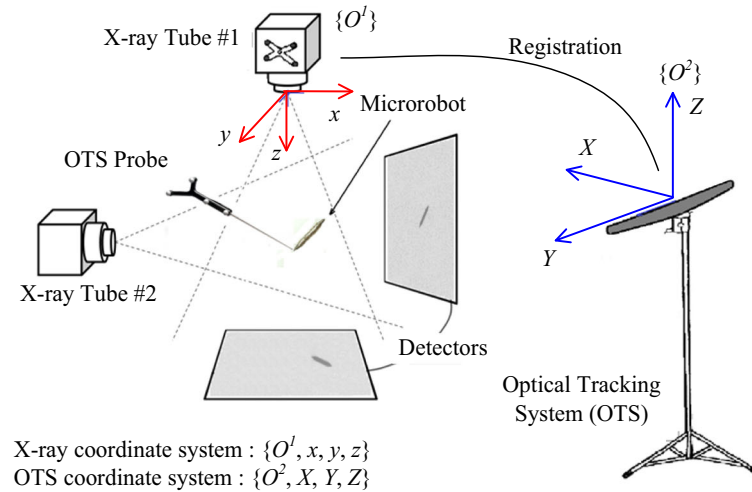
## Discussion

The efficiency of the whole tracking process could be improved by using the PCA algorithm based on the following aspects: First, since the PCA algorithm can extract the tips of the microrobot in a 2D image with high resolution, the distance error from the tips appearing in the X-ray

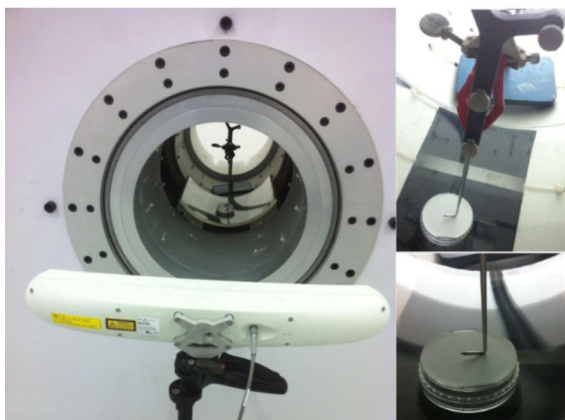
image and the tip detected by the PCA algorithm has been minimized to 3–4 pixels, as shown in Fig. 1c. Second, the total processing time to extract the feature points of a microrobot from two 2D images and a 3D X-ray reconstruction is only 0.1–0.125 ms/frame with less than 0.4 mm error. The improved efficacies are summarized in Table 2, where the reconstruction accuracy and processing time of the proposed algorithm are comparable to other relevant algorithms in [9–12]. Subsequently, the suggested method is free of additional noise-filtering algorithms against the noise and blur patterns inside raw X-ray images as in Fig. 1b. Conventionally, to handle images with noise or blur inside a specific



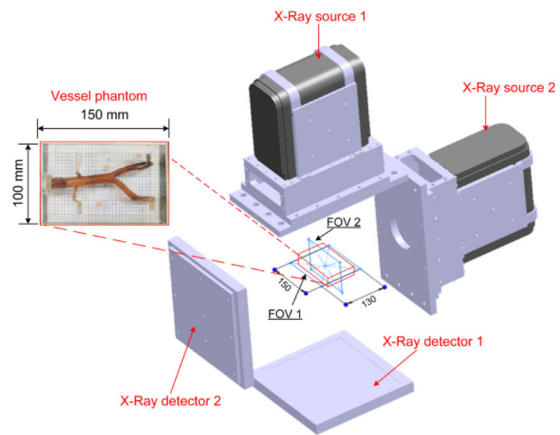
(a)



(b)



(c)



(d)

**Fig. 3** Experimental setup; **a** design and actual prototype of EMA system integrated with biplane X-ray, **b** schematics of the whole experimental setup with the coordinate system, **c** OTS measurement setup, and **d** FOV of the biplane X-ray and in vitro vascular phantom

region, several image processing techniques, such as erosion, dilation, and smoothing, are necessary. However, these methods may change the geometric shape of the region and result in an error in the reconstruction process. Nevertheless, it is

not necessary to obtain the whole perfect region or contour of the microrobot as suggested by the PCA algorithm, because the point cloud approach in the PCA algorithm is sufficient for determining the required principal components. This is a

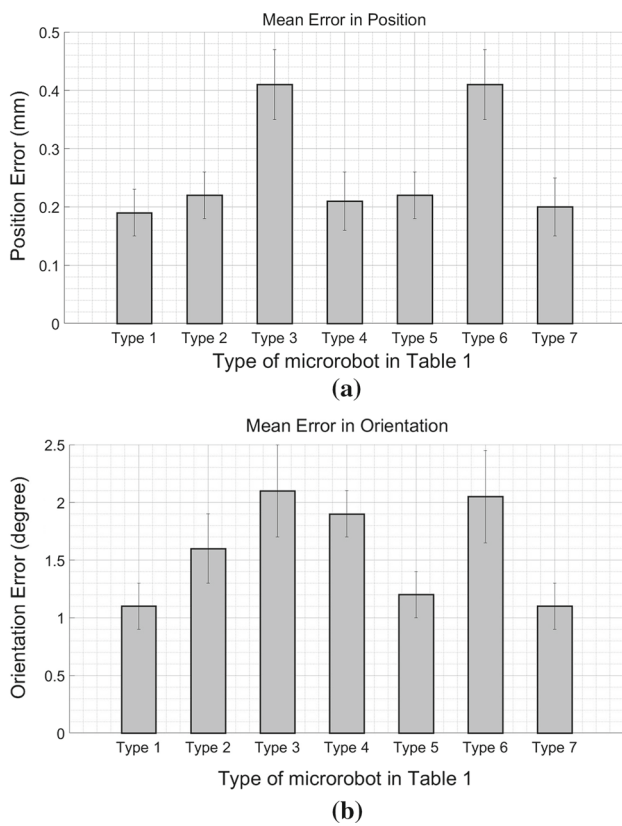


**Fig. 4** Recognition errors for the seven different types of microrobots depicted in Table 1; **a** position and **b** orientation

particular advantage of using the PCA algorithm compared to other image processing techniques.

As a consequence of the image processing analysis and experiments in this study, we were able to specify the trackable geometric shape of the microrobots, for better X-ray imaging precision in intravascular treatment, as follows: (1) the shape of a cylinder, a spiral, or any shape with uniform distribution of material along its longitudinal axis is necessary because the PCA algorithm is suitable for analyzing a symmetric distribution along the major and minor axes, (2) the longitudinal axis needs to be a straight line to be fitted with the two component axes, (3) the cone-shaped tips with an open (or vertex) angle  $\alpha$  of less than  $30^\circ$  is sufficient to minimize the error, and (4) the material should be made of metal or have a metal coil, gutta-percha, or any type of radiation-opaque material that can be easily detected by an X-ray machine.

There are limitations of the proposed technique, which include the microrobot size and orientation estimation. Depending on the size of the microrobot, the algorithm computation time may increase. The orientation estimation is sensitive to noise and can be responsible for increasing the error in case of poor segmentation. Further, the whole system needs to be designed by considering FOV of X-ray and ROI of EMA for the practical application to human subject in the future.

### Conclusions

In this paper, we presented a real-time microrobot 3D reconstruction technique for the spatial position and orientation of

**Table 2** Comparison of processing times and position/orientation errors with various algorithms proposed in [9–12]

Algorithm proposed by	Detail methods	Max. processing time (ms)	Absolute error in position (mm)	Absolute error in orientation ( $^\circ$ )
[9]	Biplane X-ray Grassfire algorithm + Pinhole camera model 3D position	0.005	2	N/A
[10]	Robotic US catheter Voxel-based interpolation + PT-based 3D reconstruction 3D position and orientation	30	2.2	0.8
[11]	Segmented images Learning + inference algorithm 3D orientation	N/A	N/A	16.7
[12]	Two high-speed visions 3D self-windowing algorithm 3D position and orientation	1	60	2–8
Our method	Biplane X-ray Clouding + PCA 3D position and orientation	0.125	0.2–0.4	1–2

the microrobot for intravascular therapeutic purposes. The PCA algorithm and X-ray reconstruction methods are suggested and utilized to accomplish a high efficacy of the 3D micro-sized object reconstruction. The results showed that the extraction of both the spatial position and orientation of the microrobot can be achieved with high accuracy. Since the processing time of the suggested method was less than 0.1 ms for the PCA algorithm and 0.025 ms for the X-ray reconstruction, the suggested method can be implemented on a real-time microrobot tracking system. Furthermore, the reconstruction accuracy was small enough to recognize the microrobot shape in the intravascular. Future work will include the application of the suggested algorithm to the catheter tip, capsule endoscope, and drug delivery carrier to advance the medical microrobot system development.

**Funding** This research was supported by the Bio & Medical Technology Development Program of the National Research Foundation (NRF) funded by the Korean government (MSIT) (No. 2015M3D5A1065682). Seong Young Ko, for this work, was supported by the Basic Science Research Program through the National Research Foundation of Korea (NRF) funded by the Ministry of Education (NRF-2016R1D1A1B03933079).

## Compliance with ethical standards

**Conflict of interest** The authors declare that they have no conflicts of interest.

**Ethical approval** This article does not contain any studies, performed by any of the authors, with human participants or animals.

**Informed consent** This article does not contain patient data.

## References

- World Health Organization (2015) Noncommunicable diseases progress monitor 2015
- Dharmarajah B (2015) European Congress of Radiology, p 1
- Bashir R, Zack CJ, Zhao H, Comerota AJ, Bove AA (2014) Comparative outcomes of catheter-directed thrombolysis plus anticoagulation vs anticoagulation alone to treat lower-extremity proximal deep vein thrombosis. *JAMA Intern Med* 174:1494–1501. <https://doi.org/10.1001/jamainternmed.2014.3415>
- Bowdle A (2014) Vascular complications of central venous catheter placement: evidence-based methods for prevention and treatment. *J Cardiothorac Vasc Anesth* 28:358–368
- Nelson BJ, Kaliakatsos IK, Abbott JJ (2010) Microrobots for minimally invasive medicine. *Annu Rev Biomed Eng* 12:55–85. <https://doi.org/10.1146/annurev-bioeng-010510-103409>
- Belharet K, Folio D, Ferreira A (2010) 3D MRI-based predictive control of a ferromagnetic microrobot navigating in blood vessels. In: 2010 3rd IEEE RAS and EMBS international conference on biomedical robotics and biomechanics, BioRob 2010, pp 808–813
- Climent J, Hessel RA (2012) Particle filtering in the Hough space for instrument tracking. *Comput Biol Med* 42:614–623. <https://doi.org/10.1016/j.compbiomed.2012.02.007>
- Lugez E, Sadjadi H, Joshi CP, Akl SG, Fichtinger G (2017) Improved electromagnetic tracking for catheter path reconstruction with application in high-dose-rate brachytherapy. *Int J Comput Assist Radiol Surg* 12:681–689
- Oh J, Park JO, Park S, Ko SY (2015) Image-based guidance system for intravascular microrobot: Fiducial marker-based registration using biplanar fluoroscopic images and CTA images. In: 2015 15th international conference on control, automation and systems (ICCAS), pp 919–922
- Brattain LJ, Loschak PM, Tschabrunn CM, Anter E, Howe RD (2014) Instrument tracking and visualization for ultrasound catheter guided procedures. In: Augmented environments for computer-assisted interventions, pp 41–50
- Saxena A, Driemeyer J, Ng AY (2009) Learning 3-d object orientation from images. In Robotics and Automation. In: ICRA'09. 2009 IEEE international conference on robotics and automation, pp 794–800
- Nakabo Y, Ishi I, Ishikawa M (2002) 3D tracking using two high-speed vision systems. In: Proceedings of IEEE/RSJ international conference on intelligent robots and systems, pp 360–365
- Tognarelli S, Castelli V, Ciuti G, Di Natali C, Sinibaldi E, Dario P, Menciassi A (2012) Magnetic propulsion and ultrasound tracking of endovascular devices. *J Robot Surg* 6:5–12. <https://doi.org/10.1007/s11701-011-0332-1>
- Iaquinto JM, Kindig MW, Haynor DR, Vu QB, Pepin N, Tsai R, Sangeorzan BJ, Ledoux WR (2018) Model-based tracking of the bones of the foot: a biplane fluoroscopy validation study. *Comput Biol Med* 92:118–127. <https://doi.org/10.1016/j.compbiomed.2017.11.006>
- Fitzgibbon A, Pilu M, Fisher RB (1999) Direct least square fitting of ellipses. *IEEE Trans Pattern Anal Mach Intell* 21:476–480. <https://doi.org/10.1109/34.765658>
- Benjamin JR, Jayasree T (2018) Improved medical image fusion based on cascaded PCA and shift invariant wavelet transforms. *Int J Comput Assist Radiol Surg* 13:229–240
- Wijewickrema SNR, Paplinski AP (2005) Principal component analysis for the approximation of a fruit as an ellipse. In: Proceedings of 13th international conference central Europe on computer graphics, visualization and computer vision, pp 1–6
- Baur C, Milletari F, Belagiannis V, Navab N, Fallavollita P (2016) Automatic 3D reconstruction of electrophysiology catheters from two-view monoplane C-arm image sequences. *Int J Comput Assist Radiol Surg* 11:1319–1328
- Nguyen PB, Park JO, Park S, Ko SY (2016) Medical micro-robot navigation using image processing-blood vessel extraction and X-ray calibration. In Proceedings of the IEEE RAS and EMBS international conference on biomedical robotics and biomechanics, vol 2016, pp 365–370
- Richard Hartley AZ (2004) Multiple view geometry in computer vision. Cambridge University Press, Cambridge
- Jeong S, Choi H, Go G, Lee C, Lim KS, Sim DS, Jeong MH, Ko SY, Park JO, Park S (2016) Penetration of an artificial arterial thromboembolism in a live animal using an intravascular therapeutic microrobot system. *Med Eng Phys* 38:403–410
- Mönnich H, Stein D, Raczkowski J, Wörn H (2010) An automatic and complete self-calibration method for robotic guided laser ablation. In: Proceedings of IEEE international conference on robotics and automation, pp 1086–1087
- Horn BKP (1987) Closed-form solution of absolute orientation using unit quaternions. *J Opt Soc Am A* 4:629. <https://doi.org/10.1364/JOSAA.4.000629>
- Stein D, Moennich H, Raczkowski J, Woern H (2009) IEEE automatic and hand guided self-registration between a robot and an optical tracking system. In: ICAR 2009 14th international conference on advanced robotics, vol 1–2, pp 13–17